

An investigation of the ballistic performance of independent ceramic target

M.K. Khan^a, M.A. Iqbal^{a,*}, V. Bratov^{b,c}, N.F. Morozov^{b,c}, N.K. Gupta^d

^a Department of Civil Engineering, Indian Institute of Technology Roorkee, Roorkee, 247667, India

^b Institute for Problems in Mechanical Engineering, Russian Academy of Sciences, Saint Petersburg, Russia

^c Department of Theory of Elasticity, Saint Petersburg State University, Saint Petersburg, Russia

^d Department of Applied Mechanics, Indian Institute of Technology Delhi, New Delhi-110016, India

ARTICLE INFO

Keywords:

Ballistic resistance
Bare ceramic target
Fragmentation
Alumina 99.5%
Steel 4340

ABSTRACT

The ballistic experiments have been carried out on alumina 99.5% bare ceramic plates for studying the initiation and propagation of brittle fracture and the resistance offered by the target. The ceramic tiles of size, 100 mm × 100 mm, and thickness, 5 mm, were impacted by the ogival nosed hardened steel 4340 projectiles of diameter 10.9 mm and mass 30 grams at velocities in the range 52–275 m/s. The ceramic fragments were carefully collected to examine the cracking patterns at the front and the back surfaces. The cracks developed in the target were studied extensively to develop more insight into the fracture mechanism. The energy absorbed by the target has been studied and correlated with respect to the fracture mechanism of the target. Numerical simulations have been performed on a commercial finite element code and the experimental findings have been reproduced in order to further understand the fracture and fragmentation behaviour and its influence thereon the ballistic characteristics of the target. The Johnson-Holmquist-2 (JH-2) constitutive model has been used for simulating the material behaviour of ceramic and the Johnson-Cook (JC) elasto-viscoplastic material model for simulating the behaviour of the steel projectile. The behaviour of ceramic target under oblique impact was explored numerically. The damage in the projectile was found to be higher in case of oblique impact. Both the experimental and numerical findings have described an increase in the crack density with the increase in the incidence velocity of the projectile. The average size of the fragments has also been found to be reduced with the increase in the projectile incidence velocity.

1. Introduction

The primary requirements for an armour material are low density, high strength and high ductility. Ceramics have emerged as one of the most suitable armour materials due to their low density, high compressive strength and high hardness. A relatively low fracture toughness and less tensile strength however ceases the possibility of using the ceramic as an independent armor structure. However, in spite of the associated limitations responsible for a premature fracture, the ceramic when used as the front layer of a composite armour with a ductile backing is considered to be most effective in defeating the armor piercing projectile. The function of ceramic layer is to shatter or blunt the projectile and thus restrict the perforation process. Although, the ceramic front layer is completely fractured during this process, the backing layer helps in keeping the comminuted ceramic in position for further energy dissipation. The remaining kinetic energy of projectile is subsequently absorbed in the plastic deformation of the backing plate.

The ductile backing thus serves as the reinforcement imparting ductility and tensile strength to the protective system [1,2]. The ballistic performance of ceramic has been investigated in the available literature considering it as a front layer in a bi-layer armour. The available studies on bi-layer ceramic could be categorized based on the backing layer material as metallic bi-layer armour [3–16] and composite bi-layer armour [17–21]. The composite armor is meant to replace the traditional metallic armor as it reduces the weight of the body armor for facilitating the movement of the personnel. The light weight armour when used in military vehicles reduces the fuel consumption and ensures the safety of the vehicle by reducing the load on the underlying weaker terrain. A significant pre-eminence of ceramic based composite armour has been noticed [22] over conventional single layer metallic armor at velocities higher than 250 m/s. The design of composite armor involves determining the optimum thickness ratios of ceramic and backing plate for obtaining the best protection level at minimum weight. The armours made-up of ceramic and aluminium plates of consistent properties but

* Corresponding author.

E-mail addresses: iqbalfce@iitr.ac.in, iqbal_ashraf@rediffmail.com (M.A. Iqbal).

<https://doi.org/10.1016/j.tws.2020.106784>

Received 27 January 2020; Received in revised form 1 May 2020; Accepted 12 May 2020

Available online 6 June 2020

0263-8231/© 2020 Elsevier Ltd. All rights reserved.

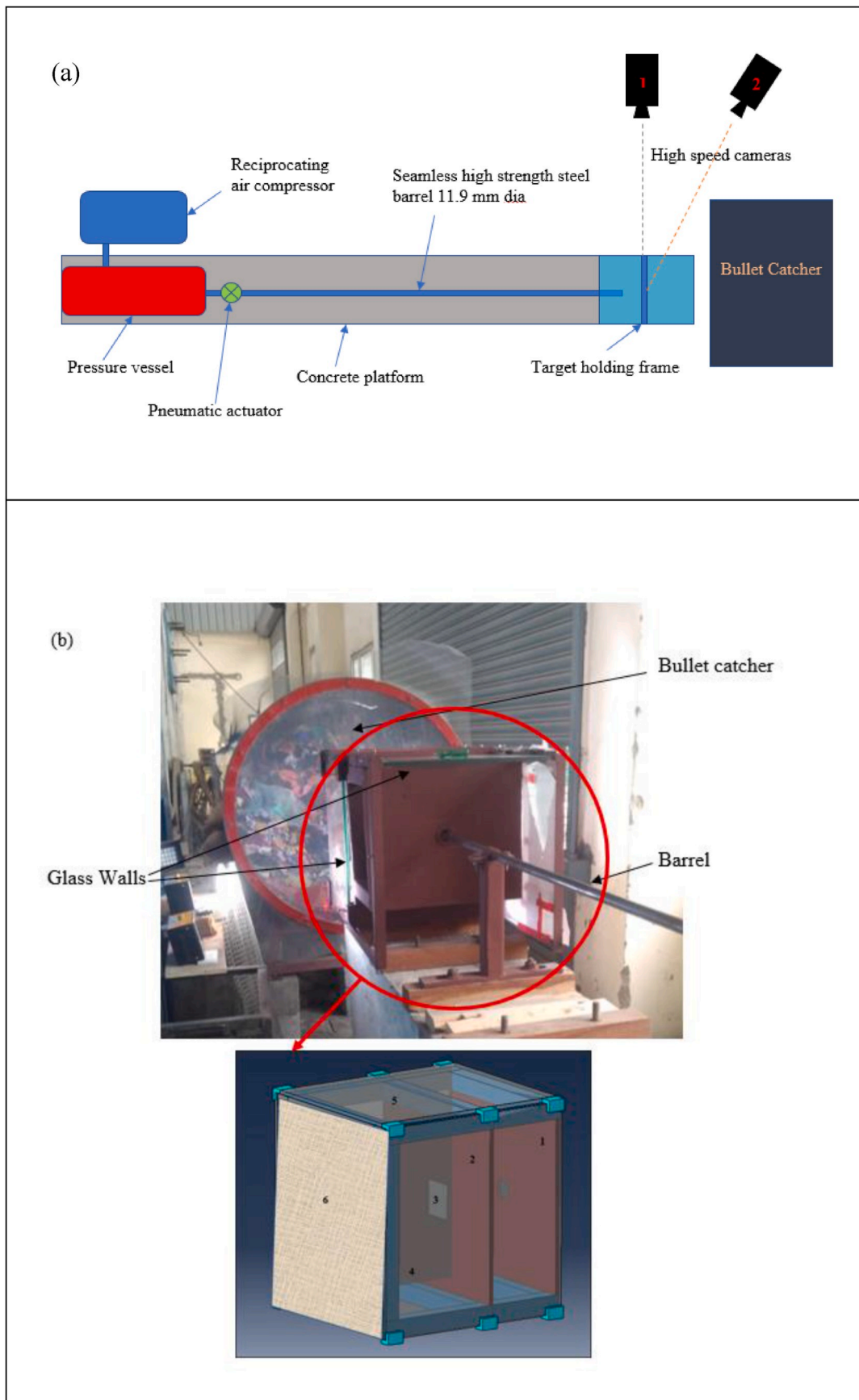


Fig. 1. (a) A schematic top view of pneumatic gun setup (b) Target holding frame with (1) Front steel plate (2) Rear steel plate (3) Slot for holding the target (4) Side thick glass panel (5) Top thick glass panel (6) Thin fabric cover.

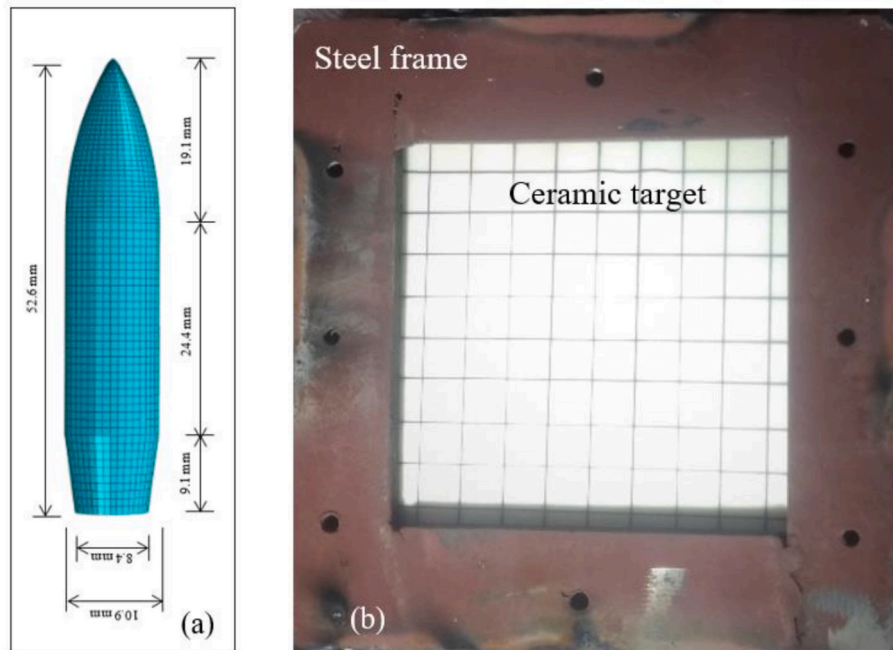


Fig. 2. (a) The schematic of the projectile (b) Ceramic target held in steel frame.

different thickness ratios have been seen to offer best performance against 7.62 mm AP projectiles when the alumina/aluminium thickness ratios were more than or equivalent to unity [3]. The theoretically optimum ratio of 2.5 has been suggested to provide an armour with near optimum performance. A combined experimental and numerical study performed by Lee and Yoo [8] on alumina/aluminium composite target against 7.62 mm AP projectiles described no significant difference in the performance of the target for the thickness ratios between 1.5 and 3. However, the optimum thickness ratio was identified as 2.5.

The studies focussing primarily on the fracture and fragmentation of the ceramic are limited in the open literature. The long rod penetration mechanism of steel encased ceramic (Al_2O_3 , SiC, B_4C and TiB_2) target at a range of incidence velocities (0.8–1.4 km/s) described that the crushing of a small volume of ceramic in the vicinity of impact zone and the subsequent flow of small fragments (in the lateral direction) constituted the major defeating target mechanism [23]. When an ogival nosed projectile strikes the hard surface of the ceramic, its nose is blunted and the resultant effective cross-sectional area is increased, causing the reduction in the compressive stress in the ceramic. The square nosed striker was seen to be more effective in penetrating the ceramic as less energy was dissipated in the deformation of the striker. When the hardness of the striker material was more than that of the ceramic, the penetration capability of ogival nosed striker is seen to have recovered subsequent to the blunting process [4]. The failure mechanism of the AD95 ceramic confined with 4340 steel under different conditions of confinement (front, side and back) described that the restraint provided against the ejection of fragments by introducing a front cover plate could substantially improve the ballistic performance in comparison to that of the restraint provided against the radial expansion [10].

The studies about the ballistic performance of ceramic based bi-layer armour are indeed important in respect of the functional utility of the ceramic, however, in order to understand and improve the contribution of ceramic in a bi-layer armour a further insight is required to be developed about the ballistic properties of the bare ceramic. The development and propagation of damage in alumina ceramic with and without a thin fiber-glass wrapping was studied by Rahbek et al. [24] at below perforation velocities against M61 7.62 mm AP projectiles. The experimental results demonstrated that the covered plates experienced

significantly more damage than that observed in the bare plates. The numerical simulations performed on LS-DYNA code successfully reproduced the cracking pattern and the damage evolution in ceramic explaining the usefulness of the restraining effect. An analytical model has been developed for predicting the behaviour of ceramic tiles without any backing plate at the useful range of incidence velocities, including below the Bernoulli limit [2]. The novel algorithm of the proposed model enables the erosion of the projectile tip when it is in contact with the target at the zero level of penetration. Thus, the capability of the model to reproduce the impact event at relatively low incidence velocities is a fundamental step towards an optimal design of the ceramic target with minimum thickness of the backing layer.

The ballistic investigation of an independent ceramic target, therefore, explains the mechanics of the evolution and propagation of damage which certainly influence its capability to defeat the projectile in a multilayer configuration and also improves understanding about the computational modelling of its structural behaviour.

A detailed experimental and numerical investigation has been reported in this manuscript on the fragmentation and ballistic evaluation of alumina 99.5% independent ceramic target against 30 grams ogival nosed hardened steel projectile at normal incidence velocities in the range, 52–275 m/s. The ceramic tile of planner dimensions, 100 mm \times 100 mm, and thickness, 5 mm, was impacted by the projectile close to and above the ballistic limit velocities. The incidence and the residual projectile velocities were measured through high speed videography. The damage induced in the target was quantified based on the number and the size of the cracks. A detailed numerical investigation has been carried out on ABAQUS/Explicit code to further explore the propagation of damage in the ceramic target. Simulations accurately reproduced the residual projectile velocities and the magnitude of damage in the target as well as the projectile. The numerical investigation was subsequently carried out to understand the performance of the ceramic against oblique impact.

2. Experiments

The ballistic experiments have been carried out in the Impact Laboratory at IIT Roorkee for studying the fragmentation behaviour of 5 mm thick alumina 99.5% targets against ogival nosed steel projectiles.

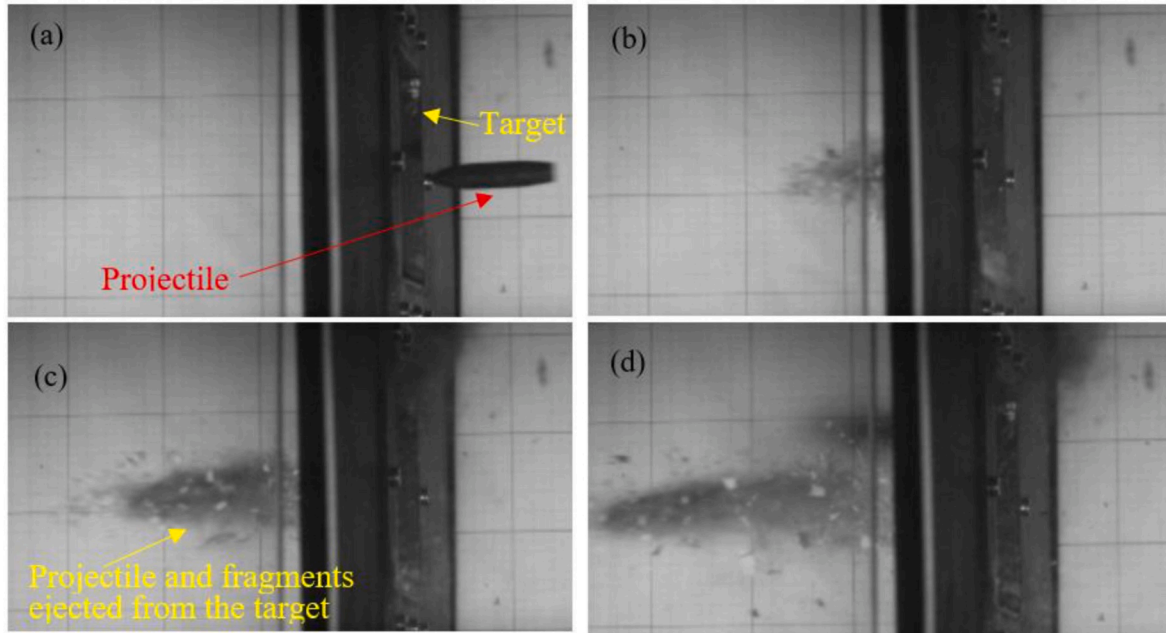


Fig. 3. Penetration process recorded by high speed camera at a velocity of 275 m/s at (a) 0, (b) 400, (c) 650 and (d) 900 μ s

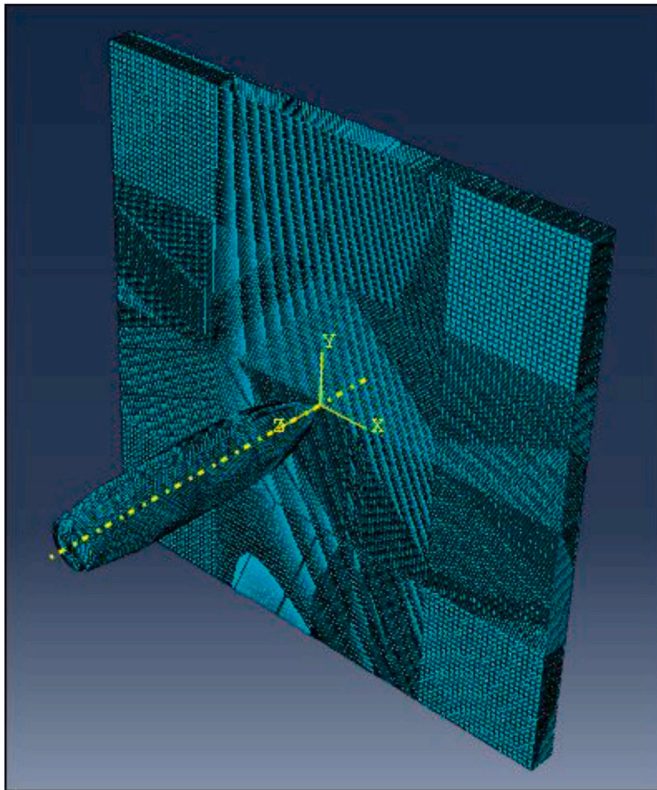


Fig. 4. Meshing of projectile and target.

The total of nine ballistic experiments were conducted by carefully varying the incidence velocity of the projectile and the response of the target corresponding to each incidence velocity was studied. The projectiles were fired with the help of a pneumatic gun shown in Fig. 1 (a). The pneumatic gun had a pressure vessel of 20-litre capacity connected to a 5 m long smooth steel barrel of inside diameter, 11.9 mm. The projectile was accelerated by instantaneously releasing the air pressure

from the vessel with the help of a pneumatic actuator. A robust target holding setup consisting of two thick steel plates {marked 1 and 2 in Fig. 1(b)} supported on a rigid steel frame was designed. The purpose of the front steel plate (1) was to arrest the fragments ejected from the front surface of the target and it was provided just at the muzzle end with a central hole of diameter, 50 mm. The rear steel plate (2) provided at a distance of 200 mm from the front plate (1) had a slot for holding the target {marked 3 in Fig. 1(b)} of span, 100 mm \times 100 mm. After inserting the ceramic tile in the slot, the edges of the plate were tightened for arresting the movement of plate and maintaining fixity at the supports. The clear span of the tile was 95 mm \times 95 mm. The two other sides and the top of the steel frame were covered with the thick glass panels. The glass panels providing a transparent shield between the two steel plates helped in recovering the fragments ejected from the front surface of the target without obstructing the view for the high speed camera. The space behind the rear steel plate was also covered by fixing the side as well as the top glass panels onto the rigid steel frame. The transparent glass panels facilitated the recovery of the fragments ejected from the rear surface of the ceramic target without obstructing the view for the high speed video recording of the projectile perforation {marked as 4 and 5 in Fig. 1(b)}. The far end of the steel frame was covered with a very thin fabric to avoid any possibility of missing the ejected fragments.

Two Phantom V411 high-speed cameras were installed to record the perforation phenomenon and to measure the projectile velocity. One of the high speed video camera (Camera-1) was placed normal to the line of sight of the projectile in front of the target holding (rear) steel plate to record the perforation phenomenon and to measure the incidence and residual velocities, see Fig. 1 (a). The second camera (Camera-2) was focused at the back surface of the target to record the damage propagation and the ejection of the fragments from the target. The frame rate of both the high speed cameras was maintained between 40,000–50,000 per second with a resolution of 500 \times 150 for Camera-1 and 256 \times 256 for the Camera-2.

The schematic of the projectile is shown in Fig. 2 (a). The diameter of the projectile shank was 10.9 mm, total length 52.6 mm, and mass 30 g. The projectile was heated for 2 hours at a constant temperature, 820 $^{\circ}$ C, in a high-temperature furnace and oil quenched subsequently for obtaining the hardness, 52 HRC.

The nose of the projectile was damaged after hitting the target in all

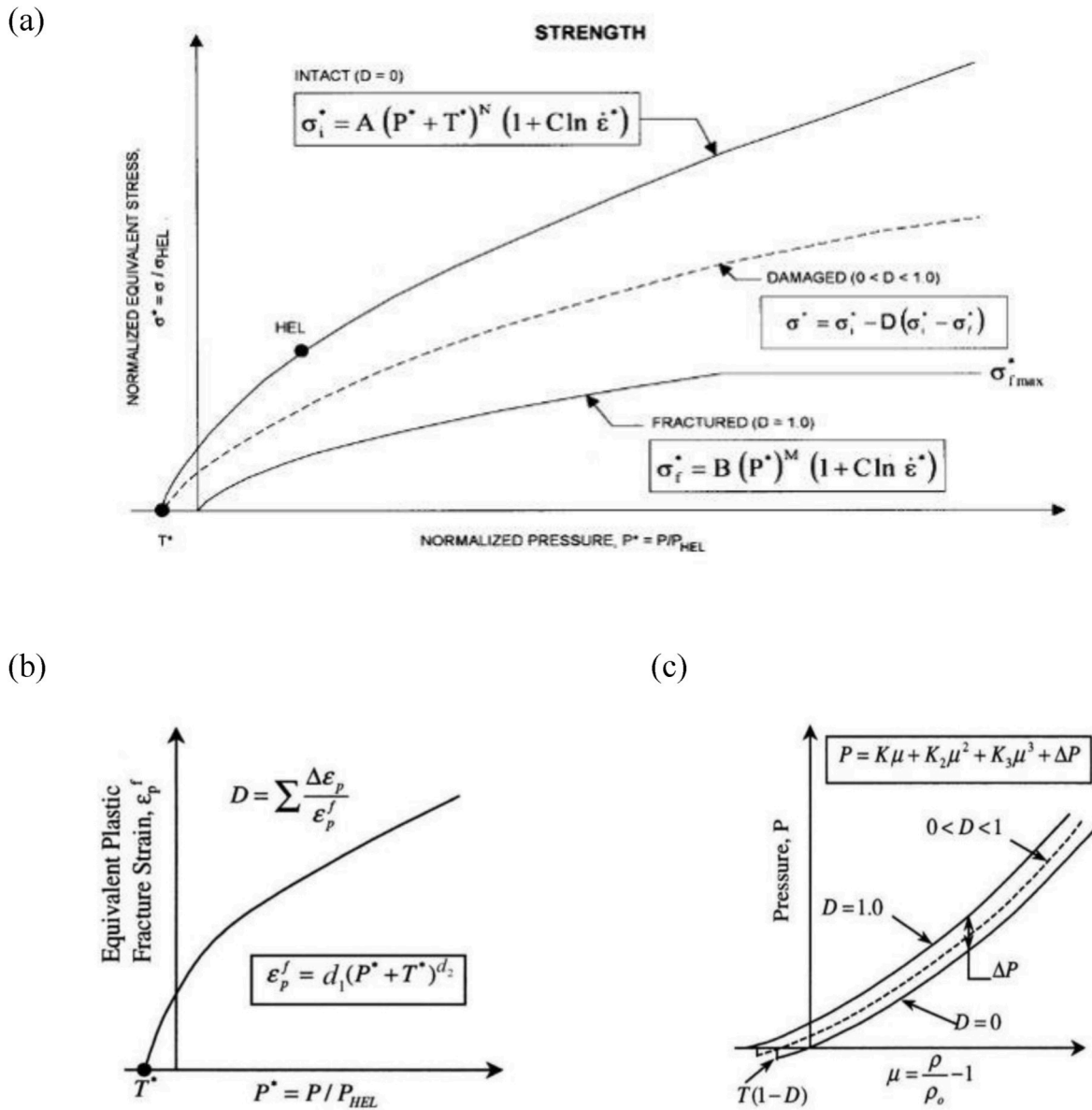


Fig. 5. (a) JH-2 Strength model (b) JH-2 Damage model (c) JH-2 Pressure model [28].

the experiments. Therefore, for each experiment a new projectile was employed. The projectile was collected after the experiment from a robust steel catcher box filled with the cotton rag. The alumina ceramic tile had its dimensions, 100 mm × 100 mm, and the thickness 5 mm, see Fig. 2 (b). The initial velocity of the projectile was varied between 52 and 275 m/s. The different stages of a typical penetration process recorded by a high speed camera at an incidence velocity of 275 m/s are shown in Fig. 3. The fragments ejected from the rear surface of the target had very high density in comparison with the fragments ejected from the front surface of the target.

3. Numerical simulation

A 3D numerical simulation model was developed using Lagrangian finite elements in ABAQUS/Explicit finite element code. Both the target and the projectiles were modeled as the deformable continuum. The central portion of the target of dimension 47.5 mm × 47.5 mm was meshed with continuum three dimensional eight node reduced integration brick elements (C3D8R) of size 0.4 mm × 0.4 mm × 0.4 mm. This is an optimum size that was identified after performing a number of

trials of numerical simulations and based on the numerical studies available in the literature [12]. The remaining portion of the target plate was meshed with continuum three dimensional eight node reduced integration (C3D8R) elements of size 0.8 mm × 0.8 mm × 0.8 mm. This configuration of elements resulted in a total number of 4,11,892 elements in the whole target of span 95 mm × 95 mm, and thickness, 5 mm. The linear C3D8R elements of size 0.4 mm × 0.4 mm × 0.4 mm was considered to discretize the body of the projectile with a total number of elements, 84,440. The finite element model of the target and projectile is shown in Fig. 4.

The interaction between the projectile and the central portion of the target was modeled using surface to surface contact with kinematic contact algorithm assuming negligible friction between the projectile and the target. This assumption was considered based on the high incidence velocity of the projectile, small target thickness and the brittle material of the target. The target plate was restrained against all degrees of freedom at its periphery.

Table 1
JH-2 constitutive model parameters for alumina 99.5% [19].

Material parameters	Numerical values
Density (kg/m ³)	3700
EOS	Polynomial
Bulk modulus, K ₁ (GPa)	130.95
Pressure constant, K ₂ (GPa)	0
Pressure constant, K ₃ (GPa)	0
Strength model	JH-2
Shear modulus, G (GPa)	90.16
Hugoniot elastic limit (HEL) (GPa)	19
Intact strength constant, A	0.93
Intact strength exponent, N	0.6
Strain rate constant, C	0
Fracture strength constant, B	0.31
Fracture strength exponent, M	0.6
Normalized maximum fractured strength, σ_{fmax}^*	0.2
Pressure at HEL (GPa)	1.46
Failure model	JH-2
Damage constant, D ₁	0.005
Damage exponent, D ₂	1
Bulking factor, β	1

Table 2
Johnson-Cook model parameters Steel 4340 [12].

Material parameters	Numerical values
Density, ρ_0 (kg/m ³)	7770
EOS	Polynomial
Bulk modulus, K ₁ (GPa)	159
Specific heat, Cr (J/KgK)	477
Strength model	JC
Shear modulus, G (GPa)	77
Static yield strength, A (GPa)	0.95
Strain hardening constant, B (GPa)	0.725
Strain hardening exponent, n	0.375
Strain rate constant, C	0.015
Thermal softening exponent, m	0.625
Melting temperature, tm (K)	1793
Reference strain rate, $\dot{\epsilon}_0$	1
Failure model	JC
Damage constant, D ₁	-0.8
Damage constant, D ₂	2.1
Damage constant, D ₃	-0.5
Damage constant, D ₄	0.002
Damage constant, D ₅	0.61

Table 3
Comparison of actual and predicted residual projectile velocities.

S. No.	Impact velocity (m/s)	Residual velocity (m/s)	
		Experiments	Simulations
1	275	239	212
2	264	215	201
3	249	182	190
4	215	153	151
5	179	116	126
6	112	70	45
7	94	58	23
8	62	31	0
9	52	26	0

3.1. Johnson and Holmquist-2 model

The Johnson-Holmquist-2 (JH-2) model [25] consisting of a polynomial equation of state (EOS), a strength model for intact, partially damaged and completely damaged material, and a damage model was employed for simulating the material behaviour of alumina 99.5%

ceramic. The polynomial equation of state (EOS) evaluated the current state of pressure as a function of volumetric change, the specific strength model provided the equivalent strength for both intact and fractured material, and the damage model was responsible for the transition of material from an intact to a fractured state. The graphical representation of the JH-2 model is provided in Fig. 5.

The normalized equivalent stress is defined as;

$$\sigma^* = \sigma_i^* - D(\sigma_i^* - \sigma_f^*) \tag{1}$$

where σ_i^* is the normalized intact equivalent stress, and σ_f^* the normalized fracture stress, and D is the damage ($0 \leq D \leq 1.0$).

The normalized intact equivalent stress is given in equation (2) and the normalized fractured equivalent stress in equation (3);

$$\sigma_i^* = A(P^* + T^*)^N (1 + C \ln \dot{\epsilon}^*) \tag{2}$$

$$\sigma_f^* = B(P^*)^M (1 + C \ln \dot{\epsilon}^*) \tag{3}$$

where A, B, C, M and N are material constants and the normalized pressure $P^* = P/P_{HEL}$ where P is the actual pressure and P_{HEL} is the pressure at Hugoniot elastic limit (HEL). The HEL is the net compressive stress corresponding to the uniaxial strain (shock wave) exceeding the elastic limit of the material. The normalized maximum tensile hydrostatic pressure is $T^* = T/P_{HEL}$, where T is the maximum tensile hydrostatic pressure the material can withstand and the dimensionless strain rate, $\dot{\epsilon}^* = \dot{\epsilon}/\dot{\epsilon}_0$, where $\dot{\epsilon}$ is actual equivalent strain rate and $\dot{\epsilon}_0$ is reference strain rate considered as 1 s^{-1} .

The hydrostatic pressure before and after the damage was expressed through equations (5) and (6), respectively;

$$P = K_1\mu + K_2\mu^2 + K_3\mu^3 \tag{4}$$

$$P = K_1\mu + K_2\mu^2 + K_3\mu^3 + \Delta P \tag{5}$$

where K₁ is a bulk modulus and K₂, K₃ are the pressure constants. The volumetric strain $\mu = \rho/\rho_0 - 1$ where ρ is current density and ρ_0 is the initial density of the material. ΔP is pressure increment due to bulking of the material due to accumulation of damage.

The damage criterion for the fracture model is same as is used in the Johnson-Cook [26,27] model;

$$D = \sum \frac{\Delta \epsilon}{\epsilon_p^f} \tag{6}$$

where $\Delta \epsilon$ is the increment in equivalent plastic strain and ϵ_p^f is the plastic strain to fracture

The plastic strain to fracture of the material is described as;

$$\epsilon_p^f = D_1 (P^* + T^*)^{D_2} \tag{7}$$

where D₁ and D₂ are the damage constants. The damage parameter D is same as is explained in the Johnson Cook model [26,27]. The details of the experiments and calculations required for the calibration of the material parameters of the JH-2 model have been discussed in Holmquist et al. [28]. The parameters of the JH-2 model for alumina 99.5% used in the present study have been directly obtained from Feli and Asgari [19], and these have been presented in Table 1.

In order to implement the JH-2 constitutive model through VUMAT program in Abaqus/Explicit code using the built-in user material, an element erosion strain (FS) is provided to remove the severely distorted elements from the mesh. It should be noted that the FS is not a material parameter but a numerical technique to smoothly run the program and to avoid severe mesh distortions during a simulation. The fine tuning of the erosion strain (FS) is a tedious process and is so carried out that the numerical computations of the material response in a simulation are not affected. When the equivalent plastic strain exceeds the given value (FS),

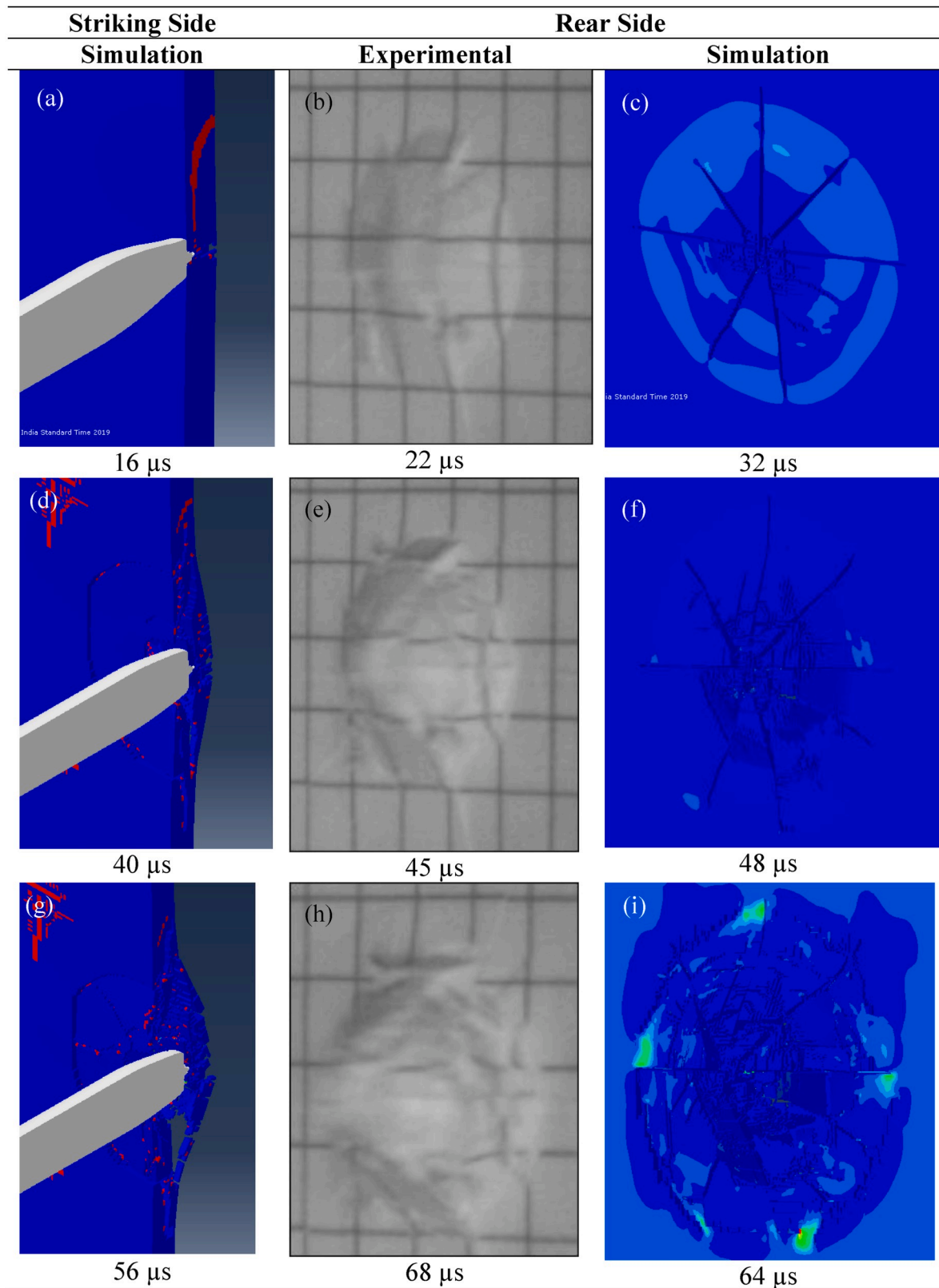


Fig. 6. The actual projectile perforation and corresponding finite element computations at different stages.

the element is removed from the mesh.

The $1Damage = 0$ is set (or left blank) to specify the JH-2 progressive damage model and $1Damage = 1$ is set to specify the JH-1 instantaneous damage model, see Abaqus Explicit User's Manual [29]. As in the present study the JH-2 constitutive model has been used, the damage has

been assumed to have increased progressively, and hence, the $1Damage = 0$ has been considered as per the requirement of the JH-2 model. Thus, the damage is assumed to occur progressively and is governed by Eqn. (6).

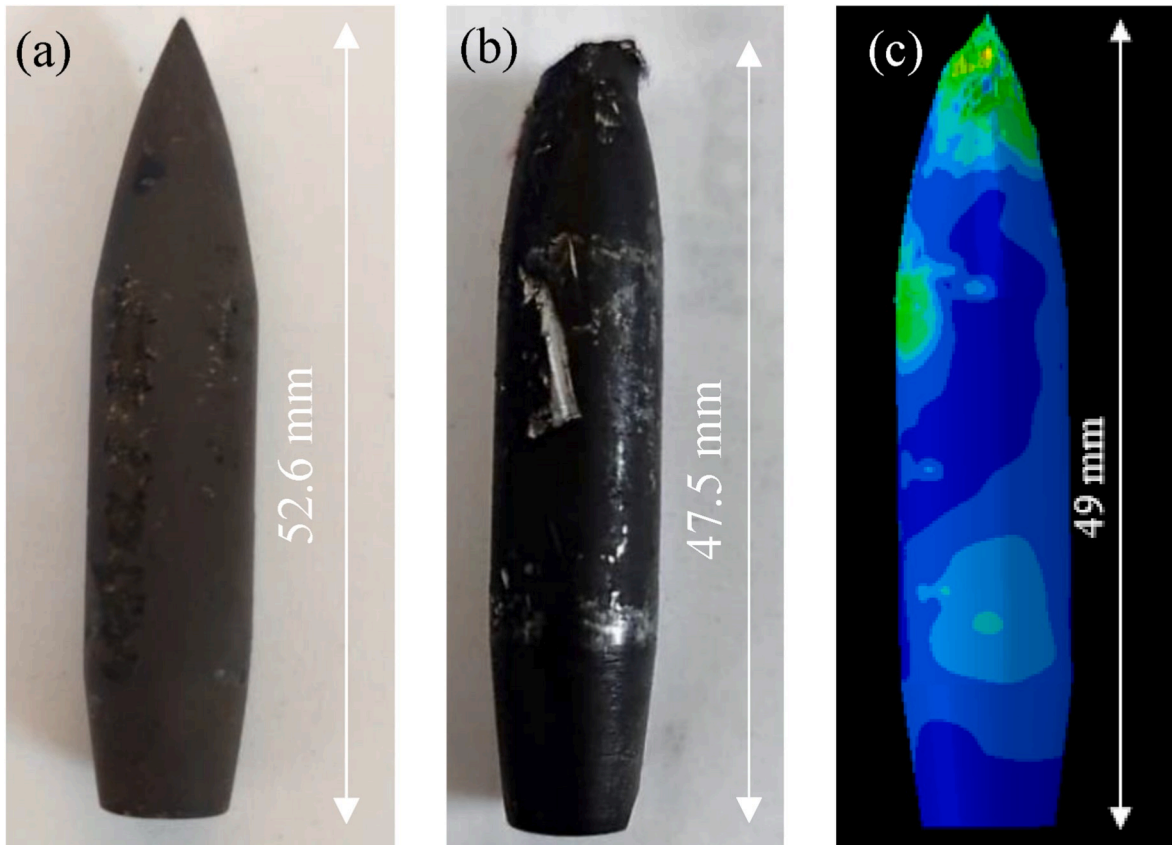


Fig. 7. The projectile (a) before experiment (b) after experiment (c) numerical result.

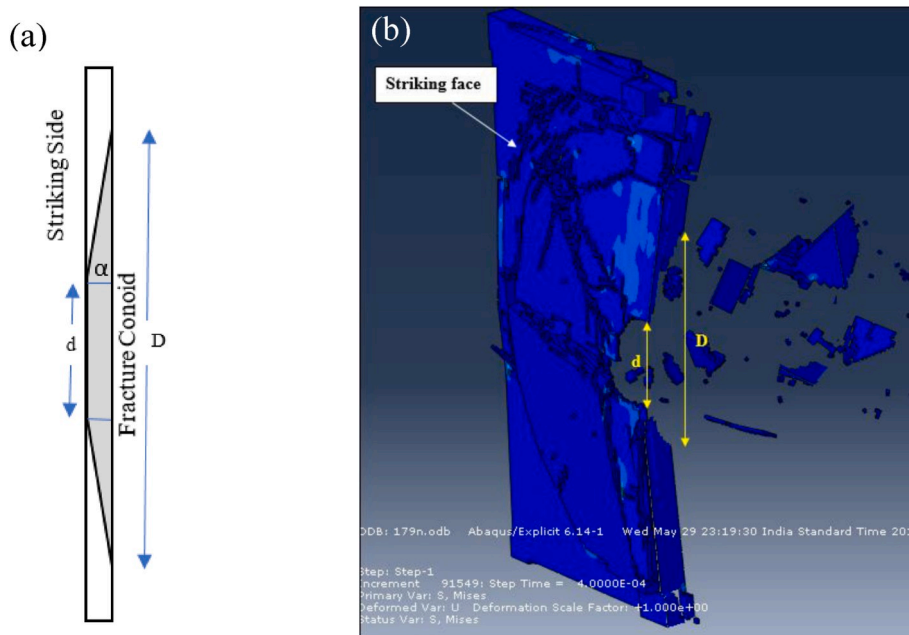


Fig. 8. (a) Schematic of the fracture conoid (b) typical fracture conoid form in the target during computer simulation.

3.2. Johnson and cook model

The Johnson-Cook (JC) constitutive model describes the behaviour of metals at large strains, high strain rates and high temperatures [26, 27]. The equivalent von-Mises stress of the Johnson-Cook model is defined as:

$$\sigma_0 = \left[A + B(\bar{\epsilon}^{pl})^n \right] \left[1 + C \ln \left(\frac{\dot{\bar{\epsilon}}^{pl}}{\dot{\epsilon}_0} \right) \right] \left[1 - \hat{T}^m \right] \quad (8)$$

where, $\bar{\epsilon}^{pl}$ is equivalent plastic strain. A, B, C, n and m are material parameters measured at or below the transition temperature, T_0 .

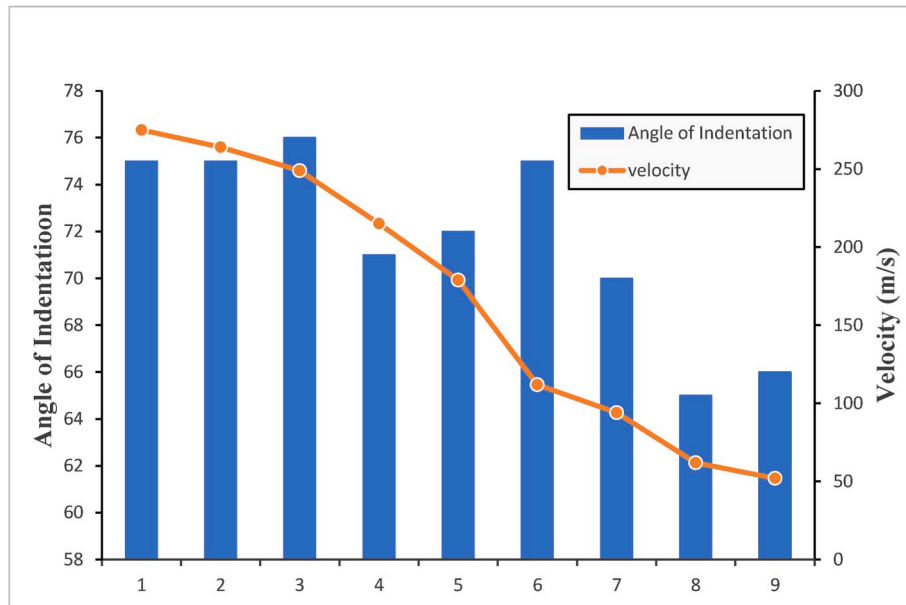


Fig. 9. Variation of the angle of indentation due to change in impact velocity.

Table 4
The damage quantification of the target with respect to impact velocity.

S. No.	Impact Velocity (m/s)	No. of radial cracks	Size of the Circumferential cone (mm)			
			Experiments		Numerical Model	
			D	d	D	d
1	52	8	34	12	-	-
2	62	7	31	10	-	-
3	94	7	39	12	48	11
4	112	9	49	11	51	12
5	179	8	44	13	42	15
6	215	7	42	13	50	14
7	249	7	52	11	47	14
8	264	8	48	11	46	13
9	275	9	52	14	59	13

\hat{T} is the non-dimensional temperature, defined as;

$$\hat{T} = \begin{cases} 0 & \text{for } T < T_0 \\ \frac{(T - T_0)}{(T_{melt} - T_0)} & \text{for } T_0 \leq T \leq T_{melt} \\ 1 & \text{for } T > T_{melt} \end{cases} \quad (9)$$

The JC fracture model is defined as;

$$D = \sum \frac{\Delta \bar{\epsilon}^{pl}}{\bar{\epsilon}_f^{pl}} \quad (10)$$

where D is the damage parameter and $\Delta \bar{\epsilon}^{pl}$ is an increment of the equivalent plastic strain and $\bar{\epsilon}_f^{pl}$ is the strain at failure.

$$\bar{\epsilon}_f^{pl} = \left[D_1 + D_2 \exp\left(D_3 \frac{\sigma_m}{\bar{\sigma}}\right) \right] \left[1 + D_4 \ln\left(\frac{\dot{\bar{\epsilon}}^{pl}}{\dot{\bar{\epsilon}}_0}\right) \right] [1 + D_5 \hat{T}] \quad (11)$$

where σ_m is the mean stress and $\bar{\sigma}$ is the equivalent von-Mises stress. $D_1 - D_5$ are the material parameters. The detailed procedure for the calibration of the material parameters for the JC model has been systematically discussed in Iqbal et al. [30]. The JC parameters for the Steel 4340 obtained directly from Ref. [12] have been provided in Table 2.

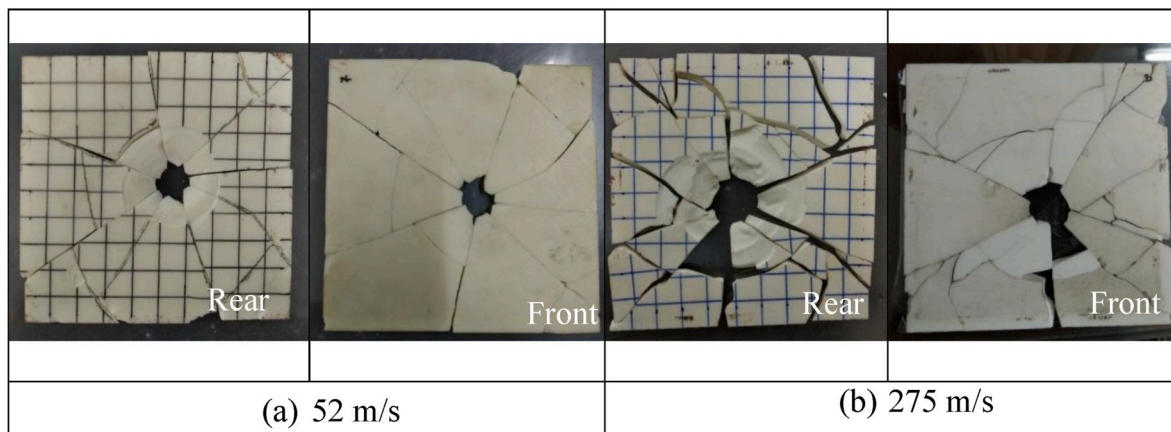


Fig. 10. Failed ceramic tiles after the impact at (a) 52 m/s and (b) 275 m/s.

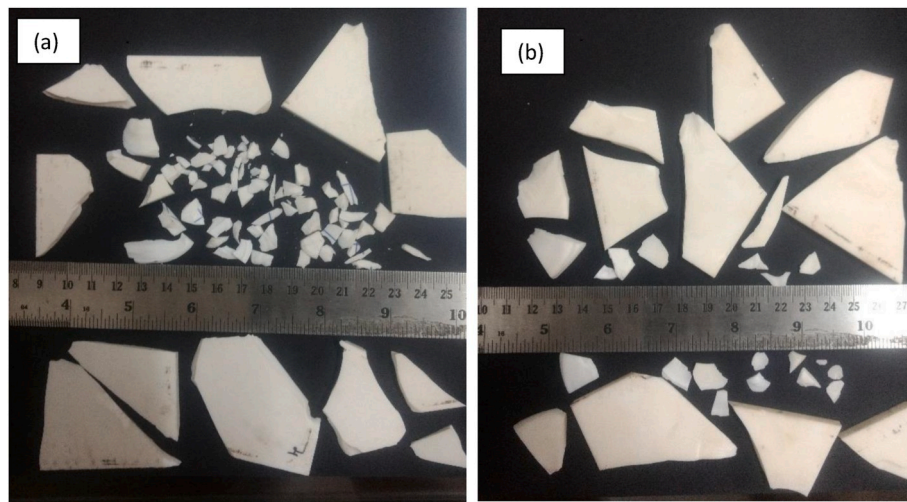


Fig. 11. The fragments of target at (a) 249 m/s and (b) 112 m/s velocity.

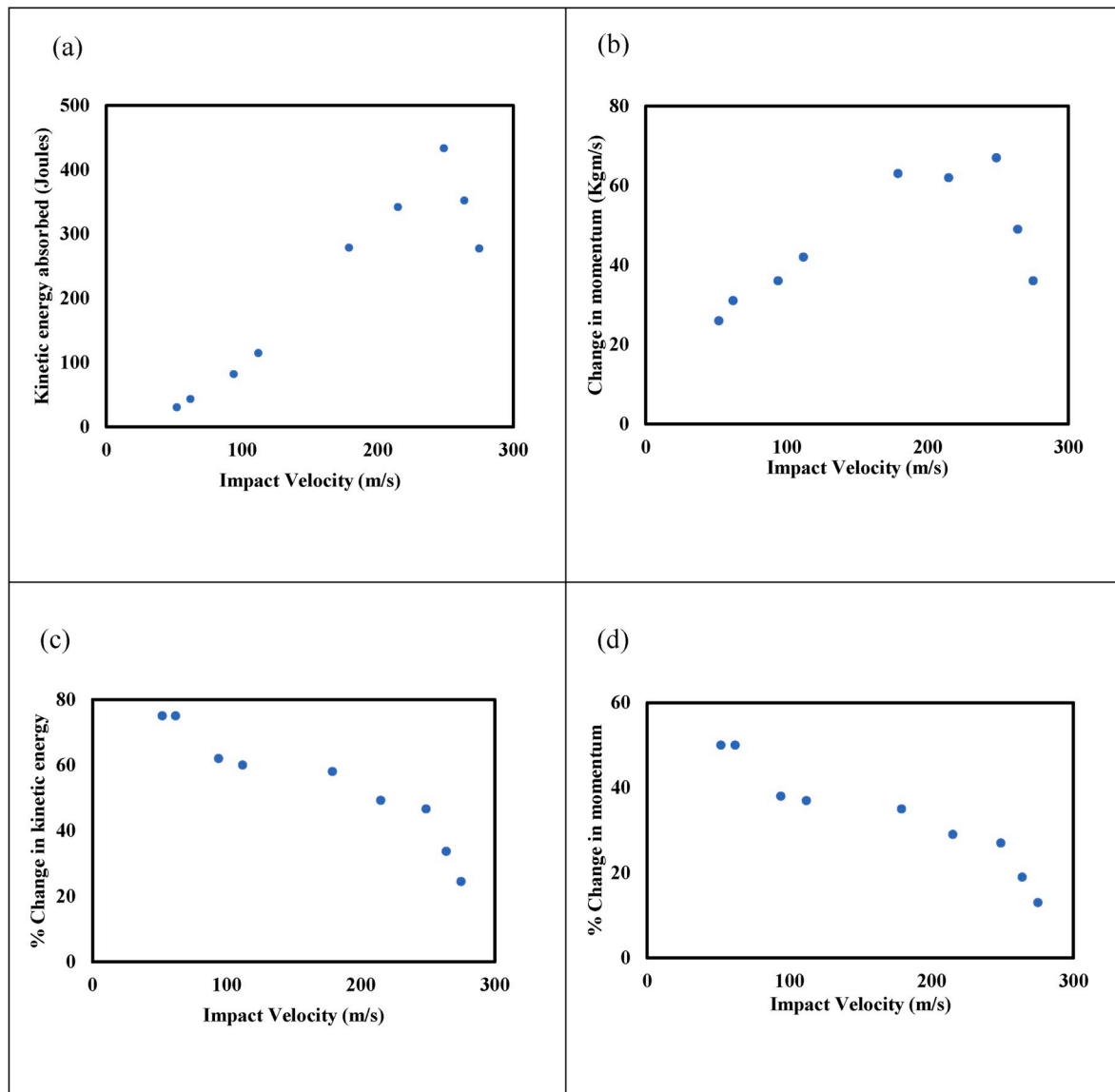


Fig. 12. (a) Variation in kinetic energy (b) Variation in momentum (c) Percentage variation in kinetic energy and (d) Percentage variation in momentum with respect to impact velocity.

Table 5

The residual velocities for normal and oblique impact for varying impact velocity.

S. No.	Impact velocity (m/s)	Residual Velocity (m/s)			
		Experimental (Normal impact)	Numerical Simulation (Obliquity)		
			0°	15°	30°
1	275	239	212	205	183
2	264	215	201	195	178
3	249	182	190	188	172
4	215	153	151	147	133
5	179	116	126	120	80
6	112	70	45	40	0
7	94	58	23	15	0

4. Impact and residual projectile velocities

The impact velocity of the projectile was varied as 52–275 m/s for studying the propagation of damage and the resultant influence on the ballistic resistance of bare ceramic target. The projectile was initially fired at a relatively high incident velocity (275 m/s) and in each subsequent experiment the velocity was reduced in order to evaluate the lowest possible velocity required for perforation of the target. However, the minimum possible velocity that was achieved through the available experimental setup for the given mass of the projectile (30 grams) was 52 m/s. The numerical simulation was performed corresponding to each ballistic test for reproducing the residual projectile velocity and the quantum of damage induced in the target. The actual and computed residual velocities compared in Table 3 described a close correlation between the experimental and numerical results. However, at incidence velocities of 62 and 52 m/s, the experiments witnessed complete perforation while the numerical simulations predicted rebounding of projectile after causing damage at the front surface of the target.

5. Damage initiation and propagation

When a projectile strikes the ceramic target, the compressive stress waves originated from the point of impact travel in the radial direction and across the thickness of the target. As the magnitude of compressive wave exceeds the dynamic strength of the ceramic, the damage initiates in the form of micro cracks leading to the comminution of ceramic in front of the projectile head. After reaching the back surface (free boundary) of the target, the compressive wave is reflected back as a tensile wave causing the formation of the circumferential tensile cracks concentric to the point of impact. With the advancement of the projectile, the compressive strength is exceeded beneath the projectile head pulverizing the ceramic and resulting in the formation of radial cracks in the outward direction from the point of impact [23].

In the present study, as the target is relatively thin and unconfined, the comminution of ceramic occurred immediately after the development of contact, see Fig. 6 (a). The projectile tip is also seen to have eroded simultaneously. The stress wave reached the back surface of the target within 24 μ s of the development of contact, causing early formation of the rear surface radial cracks, see Fig. 6 (a)–(c). With further movement of the projectile, the circumferential cracks also became visible at the back surface after 32 μ s of the contact, see Fig. 6 (d)–(f). The intersection of the radial and circumferential cracks led to the formation of the fracture conoid {Fig. 6 (g)–(i)} causing the complete failure of the target. The projectile tip is seen to be significantly distorted by the time it reached the back surface of the target, see Fig. 6 (g). The projectile recovered after each experiment was also found to have a broken tip. Fig. 7 (a) and (b) show the projectile before and after the experimentation, respectively. The average length of the recovered projectile was measured to be 47.5 mm while the average residual projectile length obtained through the numerical simulations was 49

mm, see Fig. 7 (b) and (c), respectively. Therefore, the actual and predicted average length of the broken tip was 5.1 and 3.6 mm, respectively. In a bilayer ceramic-metal (confined) target, the projectile continued penetrating the conoid located between the projectile and the backing plate causing the distribution of the momentum on the wider area of the backing plate [8] and resulting in a rapid deceleration and severe distortion of the projectile.

After each experiment, the pieces of the fractured ceramic target were placed together to measure the dimensions of the fracture conoid. The fracture conoid represents the magnitude of damage in terms of failure zone at the front and the rear surfaces. The schematic representation of the fracture conoid is provided in Fig. 8 (a). The typical numerical reproduction of the fracture conoid in the target corresponding to 179 m/s impact velocity is shown in Fig. 8 (b). The cone angle (α) of a conoid {see Fig. 8 (a)} depends upon the elastic properties of the indenter as well as ceramic material. The cone angle has been noted to be 63° for the quasi static indentation of glass plate against a spherical steel ball [31]. Florence (1965) also considered a cone angle of 63° for the analytical modelling of a bi-layer ceramic-metal target against blunt nosed projectile impact based on the assumption that the diameter of the fracture conoid is equal to the sum of projectile diameter and twice the ceramic thickness [32,33]. The experiments on the bi-layer ceramic target against ogival nosed projectile described that the cone angle is much smaller than the assumption (60–65°) considered in many analytical studies [8]. In another study, the cone angle of the bare alumina ceramic target against blunt nosed projectile impact has been reported to be 50° [34].

In the present study, the cone angle of the fracture conoid is found to be dependent upon the incidence velocity of the projectile. Though, a definite correlation could not be established, the cone angle is seen to have increased with the increase in the incidence projectile velocity, see Fig. 9. With increase in projectile velocity between 52 and 275 m/s, the cone angle increased between 65° and 76°. The fracture zones, “d” and “D”, {see Fig. 8 (a)} measured at the front and rear surfaces of the target, respectively, have been seen to increase with the increase in the projectile velocity. The measured diameter of the fracture zone at the front surface (d) varied from 10 to 14 mm and at the rear surface (D) from 31 to 52 mm. The failure mode of the ceramic target reproduced through the finite element simulations closely represented the front as well as rear surface fracture zones, see Table 4.

The number of radial cracks developed in the target have been found to increase with the increase in the projectile velocity, see Fig. 10. The circumferential cracks developed in the target have also been found to be a function of the impact velocity such that at the lowest impact velocity (52 m/s) the circumferential cracks could not be distinguished and the radial cracks played a major role in the failure of the target, Fig. 10 (a). At the highest impact velocity (275 m/s), however, several rings of the through thickness circumferential cracks emerged causing the disintegration of the target into smaller pieces, see Fig. 10 (b). Although, the magnitude and vicinity of damage in the target decreases with the increase in projectile impact velocity (due to localization of damage with increase in the strain rate), however, an opposite trend has been noticed in the ceramic targets subjected to ballistic impact not only in the present study but also in the previous studies on bare [24] and confined [12] ceramic targets.

The ejected fragments and the broken pieces of ceramic at relatively higher impact velocities have been found to be finer in comparison to those ejected at lower impact velocities. At higher impact velocities the fragments and the broken pieces of ceramic were higher in numbers and smaller in size, Fig. 11 (a), as compared to those at lower impact velocities, Fig. 9 (b). The increased fineness of the fragments at higher impact velocities was also reported by Savio et al. [35]. The high kinetic energy possessed by the projectile in case of higher velocities was suggested to be the possible reason of finer size of the debris [35].

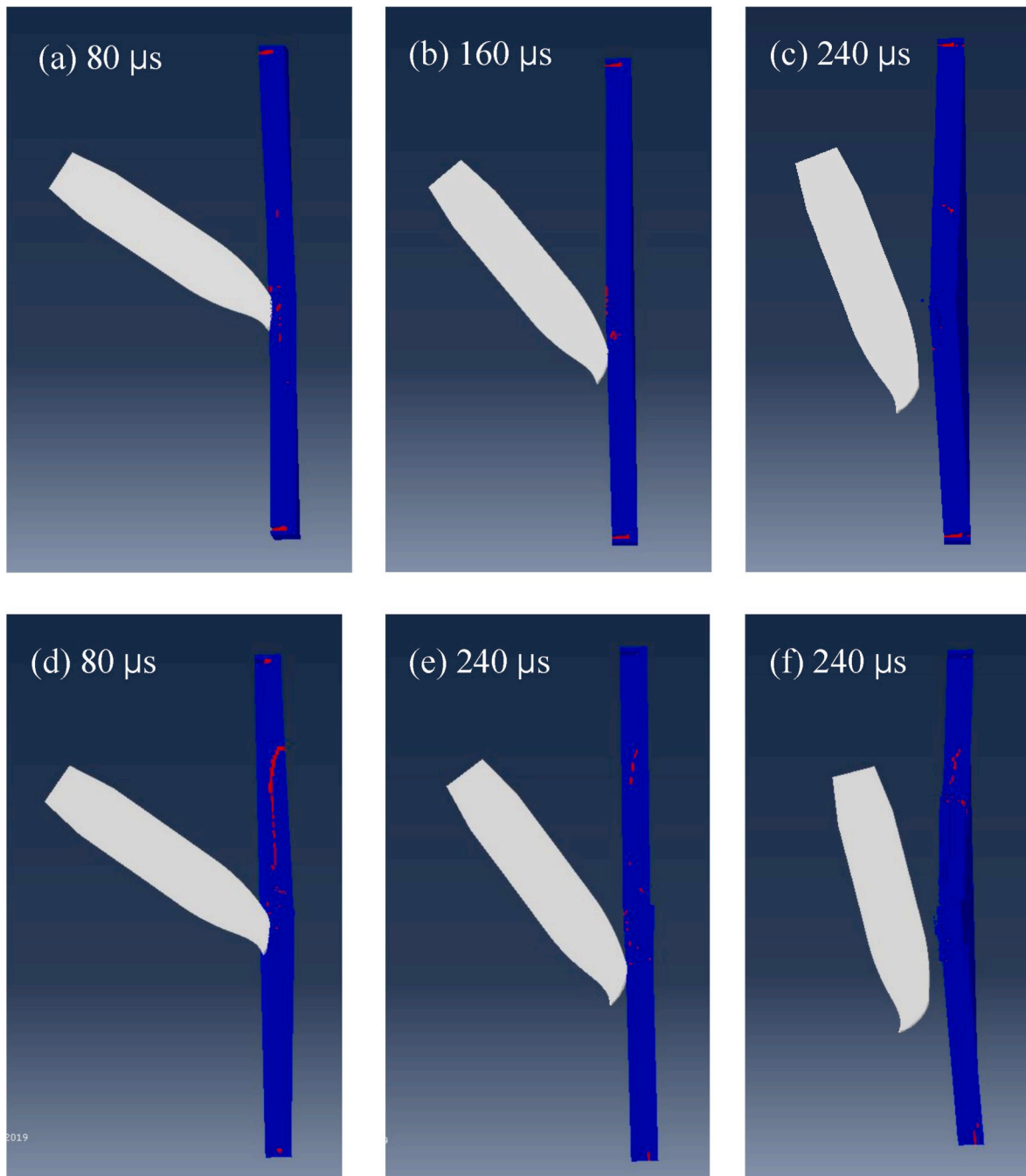


Fig. 13. Ricochet of the projectile at 30° angle of incidence at velocities 94 m/s {(a)–(c)} and 112 m/s {(d)–(f)}.

5.1. Energy dissipated by the target

The energy dissipation during projectile impact on a target could be quantified by the loss of kinetic energy during perforation. Three different hypotheses have been proposed in the literature pertaining to the energy dissipation under ballistic impact [36]. The first theory given by Florence [33] proposes that the energy absorbed by the target at an impact velocity higher than that of the ballistic limit velocity (BLV) is same as that of the energy absorbed at BLV. The analytical formulation of Recht [37] for predicting penetration in semi-infinite ductile targets against rigid projectile is based on the hypothesis that the maximum momentum transfer occurs at the just stopped condition (BLV) and that the momentum transfer actually reduces as the impact velocity increases. The projectile mass erosion model for finite thickness plate by

Tate [38] proposes that both the kinetic energy and momentum lost would increase with the increase in impact velocity subsequent to BLV. In the present study, since the mass of the eroded tip was insignificant (approximately 0.5 g), therefore, no loss of the projectile mass has been assumed for the calculation of the residual kinetic energy and momentum. The experimental results indicated that the energy absorbed by the target increased with the increase in the impact velocity up to 249 m/s. However, at the two highest impact velocities, 264 and 275 m/s, the absorbed energy has decreased, see Fig. 12 (a). The percentage loss of the absorbed energy, on the other hand, was found to decrease consistently with the increase in the impact velocity, Fig. 12 (b).

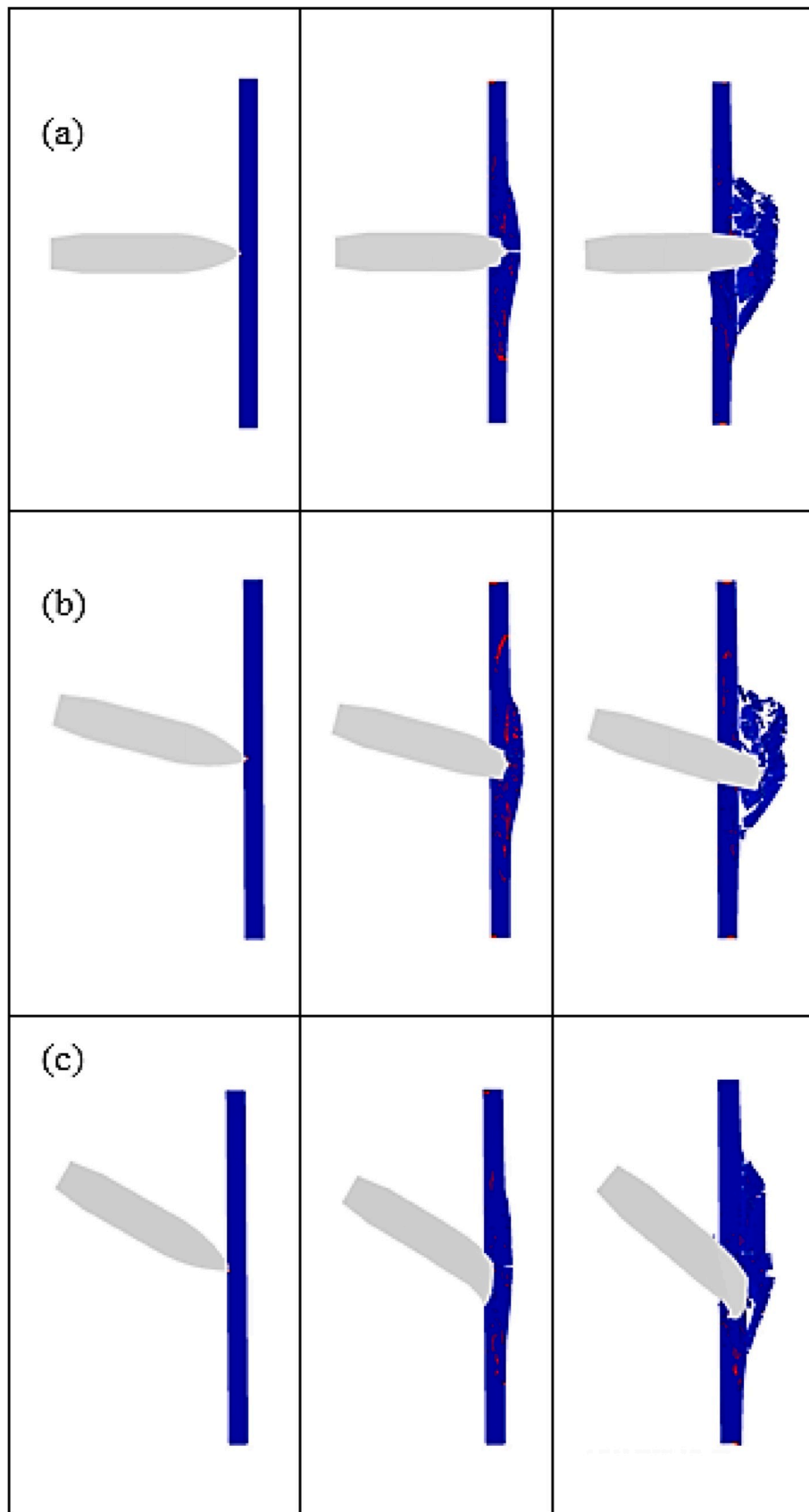


Fig. 14. Simulation results for perforation of projectile at 275 m/s impact velocity (a) Normal Impact (b) Oblique Impact at 15° (c) Oblique Impact at 30° at 5 μ s, 40 μ s and 75 μ s

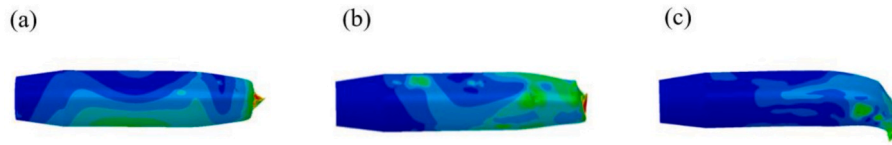


Fig. 15. The erosion of the projectile occurred at different oblique angles (a) 0° (b) 15° and (c) 30° corresponding to 275 m/s velocity.

5.2. Numerical study of oblique impact

The simulations have also been conducted by changing the angle of incidence to 15° and 30° obliquities. The incidence velocities at both the oblique angles were considered identical to what have been obtained during the experiments performed at normal incidence. The residual projectile velocities obtained at both the oblique angles have been presented in Table 5, and these have been compared with the residual velocities obtained at the normal incidence.

The residual velocities seen to have decreased with the increase in the angle of obliquity. This is due to the fact that the path length of the projectile perforation (effective target thickness) increased with the increase in the angle of obliquity resulting in the dissipation of more kinetic energy. The longer duration of interaction between the projectile and ceramic target has also led to a higher damage of the projectile. The simulations were also performed at 45° obliquity, however, the projectile did not experience perforation in the considered velocity regime. A similar increase in the ballistic resistance of bi-layer ceramic-metal [6] and ceramic-composite target [1] at oblique impact has been reported earlier by the investigators.

The reduction in residual velocity was 3% and 14% for 15° and 30° obliquity, respectively, at 275 m/s incidence velocity. At relatively lower incidence velocity, 94 m/s, the percentage reduction in the residual velocity was 35% at 15° and 100% at 30° obliquity. At 112 and 94 m/s velocities, the projectile failed to perforate at 30° obliquity and toppled down after hitting the target, see Fig. 13. The projectile experienced ricochet at both of these velocities.

The perforation process at different angles of obliquity is shown in Fig. 14 at 275 m/s velocity. The perforation path of the projectile obtained from the simulations was 5, 5.2 and 5.8 mm corresponding to 0° , 15° and 30° obliquity, respectively. The damage induced in the target as well as the projectile was higher at oblique impact and its magnitude increased with the increase in the angle of obliquity. The nose of the projectile experienced significant distortion at oblique impact, see Fig. 15. At 30° obliquity, the entire ogival nose of the projectile was eroded.

6. Conclusions

An experimental and numerical investigation was carried out to study the damage propagation and the ballistic resistance of alumina 99.5% bare ceramic target against 10.9 mm diameter ogival nosed 4340 steel projectile.

The cone angle of the fracture conoid was found to be dependent upon the incidence velocity of the projectile. Though, a definite correlation could not be established, an increase in projectile velocity from 52 to 275 m/s has described a resultant increase in the cone angle from 65° to 76° .

The number of radial cracks as well as the circumferential cracks developed in the target increased with the increase in the incidence velocity. The fragments were found to be finer at higher incidence velocities and thicker at lower incidence velocities. The numerical simulations correctly reproduced the magnitude and the pattern of damage in the target and the projectile.

The percentage loss of the absorbed energy has been found to decrease consistently with the increase in the impact velocity.

The damage induced in the target as well as the projectile increased

with the increase in angle of obliquity. The residual projectile velocities also decreased with the increase in the angle of obliquity. The effect of angle of obliquity became more prominent at relatively lower velocities such that the projectile at 30° obliquity experienced ricochet when impacted at 112 and 94 m/s.

Authors statement

M.K. Khan: Formal analysis, Methodology, Software. **M.A. Iqbal:** Conceptualization, Writing - original draft, Visualization, Project administration, Funding acquisition. **V. Bratov:** Conceptualization, Project administration, Supervision. **N.F. Morozov:** Funding acquisition, Project administration, Supervision. **N.K. Gupta,** Data curation, Visualization, Writing - review & editing

Acknowledgements

Authors gratefully acknowledge the financial support provided by the Department of Science and Technology (DST), India and Russian Foundation for Basic Research (RFBR), Russia through research grant nos. INT/RUS/RFBR/P-232, INT/RUS/RFBR/P361, 16-51-45063, 19-51-45016 for successfully carrying out this work.

References

- [1] Z. Fawaz, W. Zheng, K. Behdinan, Numerical simulation of normal and oblique ballistic impact on ceramic composite armours, Compos. Struct. 63 (2004) 387–395, [https://doi.org/10.1016/S0263-8223\(03\)00187-9](https://doi.org/10.1016/S0263-8223(03)00187-9).
- [2] L.M. Bresciani, A. Manes, M. Giglio, An analytical model for ballistic impacts against ceramic tiles, Ceram. Int. 44 (2018) 21249–21261, <https://doi.org/10.1016/j.ceramint.2018.08.172>.
- [3] J.G. Hetherington, The optimization of two component composite armours, Int. J. Impact Eng. (1992), [https://doi.org/10.1016/0734-743X\(92\)90145-J](https://doi.org/10.1016/0734-743X(92)90145-J).
- [4] B. Wang, G. Lu, M.K. Lim, Experimental and numerical analysis of the response of aluminium oxide tiles to impact loading, J. Mater. Process. Technol. 51 (1995) 321–345, [https://doi.org/10.1016/0924-0136\(94\)01604-Y](https://doi.org/10.1016/0924-0136(94)01604-Y).
- [5] V. Madhu, K. Ramanjaneyulu, T. Balakrishna Bhat, N.K. Gupta, An experimental study of penetration resistance of ceramic armour subjected to projectile impact, Int. J. Impact Eng. 32 (2006) 337–350, <https://doi.org/10.1016/j.ijimpeng.2005.03.004>.
- [6] S. Sadanandan, J.G. Hetherington, Characterisation of ceramic/steel and ceramic/aluminium armours subjected to oblique impact, Int. J. Impact Eng. 19 (1997) 811–819, [https://doi.org/10.1016/S0734-743X\(97\)00019-5](https://doi.org/10.1016/S0734-743X(97)00019-5).
- [7] R. Zaera, V. Sánchez-Gálvez, Analytical modelling of normal and oblique ballistic impact on ceramic/metal lightweight armours, Int. J. Impact Eng. 21 (1998) 133–148, [https://doi.org/10.1016/S0734-743X\(97\)00035-3](https://doi.org/10.1016/S0734-743X(97)00035-3).
- [8] M. Lee, Y.H. Yoo, Analysis of ceramic/metal armour systems, Int. J. Impact Eng. 25 (2001) 819–829, [https://doi.org/10.1016/S0734-743X\(01\)00025-2](https://doi.org/10.1016/S0734-743X(01)00025-2).
- [9] J. López-Puente, A. Arias, R. Zaera, C. Navarro, The effect of the thickness of the adhesive layer on the ballistic limit of ceramic/metal armours. An experimental and numerical study, Int. J. Impact Eng. 32 (2006) 321–336, <https://doi.org/10.1016/j.ijimpeng.2005.07.014>.
- [10] Z.H. Tan, X. Han, W. Zhang, S.H. Luo, International Journal of Impact Engineering an investigation on failure mechanisms of ceramic/metal armour subjected to the impact of tungsten projectile, Int. J. Impact Eng. 37 (2010) 1162–1169, <https://doi.org/10.1016/j.ijimpeng.2010.07.004>.
- [11] R. Chi, A. Serjouei, I. Sridhar, G.E.B. Tan, Ballistic impact on bi-layer alumina/aluminium armor: a semi-analytical approach, Int. J. Impact Eng. 52 (2013) 37–46, <https://doi.org/10.1016/j.ijimpeng.2012.10.001>.
- [12] A. Serjouei, R. Chi, Z. Zhang, I. Sridhar, Experimental validation of BLV model on bi-layer ceramic-metal armor, Int. J. Impact Eng. 77 (2015) 30–41, <https://doi.org/10.1016/j.ijimpeng.2014.11.001>.
- [13] M.J. Pawar, A. Patnaik, S.K. Biswas, U. Pandel, I.K. Bhat, S. Chatterjee, A. K. Mukhopadhyay, R. Banerjee, B.P. Babu, Comparison of ballistic performances of Al₂O₃ and AlN ceramics, Int. J. Impact Eng. 98 (2016) 42–51, <https://doi.org/10.1016/j.ijimpeng.2016.08.002>.

- [14] M.K. Khan, M.A. Iqbal, V. Bratov, N.K. Gupta, N.F. Morozov, Numerical study of fracture mechanism in ceramic armor under impact load, in: *Proc. XLVI Int. Summer Sch. Conf. APM* 2018, 2018, pp. 134–144.
- [15] M. Lee, E.Y. Kim, Y.H. Yoo, Simulation of high speed impact into ceramic composite systems using cohesive-law fracture model, *Int. J. Impact Eng.* 35 (2008) 1636–1641, <https://doi.org/10.1016/j.ijimpeng.2008.07.031>.
- [16] M.K. Khan, M.A. Iqbal, V. Bratov, N.K. Gupta, N.F. Morozov, A numerical study of ballistic behaviour of ceramic metallic bi-layer armor under impact load, *Mater. Phys. Mech.* 42 (2019) 699–710, <https://doi.org/10.18720/MPM.4262019.2>.
- [17] M.M. Shokrieh, G.H. Javadpour, Penetration analysis of a projectile in ceramic composite armor, *Compos. Struct.* 82 (2008) 269–276, <https://doi.org/10.1016/j.compstruct.2007.01.023>.
- [18] K. Krishnan, S. Sockalingam, S. Bansal, S.D. Rajan, Numerical simulation of ceramic composite armor subjected to ballistic impact, *Compos. B Eng.* 41 (2010) 583–593, <https://doi.org/10.1016/j.compositesb.2010.10.001>.
- [19] S. Feli, M.R. Asgari, Finite element simulation of ceramic/composite armor under ballistic impact, *Compos. B Eng.* 42 (2011) 771–780, <https://doi.org/10.1016/j.compositesb.2011.01.024>.
- [20] D. Bürger, A. Rocha De Faria, S.F.M. De Almeida, F.C.L. De Melo, M.V. Donadon, Ballistic impact simulation of an armour-piercing projectile on hybrid ceramic/fiber reinforced composite armours, *Int. J. Impact Eng.* 43 (2012) 63–77, <https://doi.org/10.1016/j.ijimpeng.2011.12.001>.
- [21] N.K. Naik, S. Kumar, D. Ratnaveer, M. Joshi, K. Akella, An energy-based model for ballistic impact analysis of ceramic-composite armours, *Int. J. Damage Mech.* 22 (2013) 145–187, <https://doi.org/10.1177/1056789511435346>.
- [22] M. Mayselless, W. Goldsmith, S.P. Virostek, S.A. Finnegan, Impact on ceramic targets, *J. Appl. Mech.* 54 (1987), <https://doi.org/10.1115/1.3173022> introduction pg 1.
- [23] D.A. Shockey, A.H. Marchand, S.R. Skaggs, G.E. Cort, M.W. Burkett, R. Parker, Failure phenomenology of confined ceramic targets and impacting rods, *Int. J. Impact Eng.* (1990), [https://doi.org/10.1016/0734-743X\(90\)90002-D](https://doi.org/10.1016/0734-743X(90)90002-D).
- [24] D.B. Rahbek, J.W. Simons, B.B. Johnsen, T. Kobayashi, D.A. Shockey, Effect of composite covering on ballistic fracture damage development in ceramic plates, *Int. J. Impact Eng.* 99 (2017) 58–68, <https://doi.org/10.1016/j.ijimpeng.2016.09.010>.
- [25] G.R. Johnson, T.J. Holmquist, An improved computational constitutive model for brittle materials, in: *AIP Conf. Proc.*, 1994, <https://doi.org/10.1063/1.46199>.
- [26] G.R. Johnson, W.H. Cook, Fracture characteristics of three metals subjected to various strains, strain rates, temperatures and pressures, *Eng. Fract. Mech.* 21 (1985) 31–48, [https://doi.org/10.1016/0013-7944\(85\)90052-9](https://doi.org/10.1016/0013-7944(85)90052-9).
- [27] G.R. Johnson, W.H. Cook, A constitutive model and data for metals subjected to large strains, high strain rates and high temperatures, in: *7th Int. Symp. Ballist.*, 1983, <https://doi.org/10.1038/nrm3209>.
- [28] T.J. Holmquist, D.W. Templeton, K.D. Bishnoi, Constitutive modeling of aluminum nitride for large strain, high-strain rate, and high-pressure applications, *Int. J. Impact Eng.* (2001), [https://doi.org/10.1016/S0734-743X\(00\)00046-4](https://doi.org/10.1016/S0734-743X(00)00046-4).
- [29] *ABAQUS/explicit User's Manual*, 2010, version 6.10.
- [30] M.A. Iqbal, K. Senthil, P. Bhargava, N.K. Gupta, The characterization and ballistic evaluation of mild steel, *Int. J. Impact Eng.* 78 (2015) 98–113, <https://doi.org/10.1016/j.ijimpeng.2014.12.006>.
- [31] C.G. Knight, M.V. Swain, M.M. Chaudhri, Impact of small steel spheres on glass surfaces, *J. Mater. Sci.* 12 (1977) 1573–1586.
- [32] J.G. Hetherington, B.P. Rajagopalan, An investigation into the energy absorbed during ballistic perforation of composite armours, *Int. J. Impact Eng.* 11 (1991) 33–40, [https://doi.org/10.1016/0734-743X\(91\)90029-F](https://doi.org/10.1016/0734-743X(91)90029-F).
- [33] A.L. Florence, *Interaction of Projectiles and Composite Armor Part II*, 1969, pp. 1–69.
- [34] S. Sarva, S. Nemat-Nasser, J. McGee, J. Isaacs, The effect of thin membrane restraint on the ballistic performance of armor grade ceramic tiles, *Int. J. Impact Eng.* 34 (2007) 277–302, <https://doi.org/10.1016/j.ijimpeng.2005.07.006>.
- [35] S.G. Savio, K. Ramanjaneyulu, V. Madhu, T.B. Bhat, An experimental study on ballistic performance of boron carbide tiles, *Int. J. Impact Eng.* 38 (2011) 535–541, <https://doi.org/10.1016/j.ijimpeng.2011.01.006>.
- [36] J.G. Hetherington, Energy and momentum changes during ballistic perforation, *Int. J. Impact Eng.* 18 (1996) 319–337, [https://doi.org/10.1016/0734-743X\(96\)89052-X](https://doi.org/10.1016/0734-743X(96)89052-X).
- [37] R.F. Recht, *Ballistic Perforation Dynamics of Armor-Piercing Projectiles*, 1967. China Lake, California.
- [38] A. Tate, *Extensions to the Hydrodynamic Theory of Penetration*, 1985. Kent.